Hydration due to high-T brittle failure within in situ oceanic crust, 30°N Mid-Atlantic Ridge

Katsuyoshi Michibayashi, Takehiro Hirose, Toshio Nozaka, Yumiko Harigane, Javier Escartin, Heike Delius, Margaret Linek, Yasuhiko Ohara

Hydration due to high-T brittle failure within *in situ* oceanic crust, 30°N Mid-Atlantic Ridge

Katsuyoshi Michibayashi [a,*], Takehiro Hirose [b], Toshio Nozaka [c], Yumiko Hariagane [a], Javier Escartin [d], Heike Delius [e], Margaret Linek [f], Yasuhiko Ohara[g]

[a] *Institute of Geosciences, Shizuoka University, Shizuoka 422-8529, Japan*
[b] *Kochi Institute for Core Sample Research, JAMSTEC, Kochi 783-8502, Japan*
[c] *Department of Earth Sciences, Okayama University, Okayama 700-8530, Japan*
[d] *Marine Geosciences, CNRS/IPGP, 75252 Paris, France*
[e] *Department of Geology, University of Leicester, Leicester LE1 7RH, UK*
[f] *Angewandte Geophysik, RWTH, Aachen University, Aachen 52064, Germany*
[g] *Ocean Research Laboratory, Hydrographic Department of Japan, Tokyo, Japan*

* Corresponding author: Fax: +81 54 238 4788, sekmich@ipc.shizuoka.ac.jp

Re-submitted to Earth and Planetary Sciences Letters 11th August 2008

Abstract

Analysis of an *in situ* fault zone within the Atlantis Massif oceanic core complex (Mid-Atlantic Ridge) provides clues to the relevant deformation mechanisms and their temporal evolution within oceanic crust. IODP EXP304/305 drilled a succession of gabbroic lithologies to a final depth of 1415 meters below the sea floor (mbsf), with very high recovery rates of up to 100% (generally ~80%). We identified an intra-crustal fault zone between 720 and 780 mbsf in a section of massive gabbro, olivine gabbro, oxide gabbro units, and minor diabase intrusions. Of particular interest is the section between 744 and 750 mbsf, which unfortunately was marked by low recovery rates (17%). Electrical borehole-wall images show a 1-m-thick zone of east-dipping fractures within this interval, which is otherwise dominated by N–S dipping structures. Despite the high fracture density in this section, the hole walls are smooth, with rare breakouts, suggesting that the low recovery rate was due to a change in lithology rather than well conditions. The recovered rocks include ultracataclasite and possibly incohesive fault gouge that formed in the upper amphibolite regime, with mostly amphibole infill. Logging data suggest that the gabbroic rocks in this interval are rich in hydrous phases, consistent with increased amounts of amphibole found in the core. Equilibration temperature conditions of about 640°C were obtained for plagioclase clasts and aluminous actinolite, assuming a pressure of 200MPa. The permeability of the fault zone is in the range of 10^{-19} to 10^{-17} m^2. Although the permeability appears to be high within the fault zone relative to other parts of the section, it is no higher than that in typical lower crustal material. As a consequence, because brittle failure occurred at high temperatures, the fault zone was subsequently completely sealed by hydrous minerals, thereby preventing further fluid circulation and preserving water in the crust.

Key words: IODP U1309D, Mid-Atlantic Ridge, gabbro, fault, permeability, core-log

1. Introduction

Water exists in oceanic crust within a number of hydrous minerals. When an oceanic plate subducts at a trench, the hydrated crust carries water in the form of hydrous meta-basalt (e.g., blueschist; Peacock, 1993). The hydrous minerals become unstable at the pressures and temperatures of the shallow subduction zone (~50 km depth) and are dehydrated to produce anhydrous eclogitic oceanic crust. This dehydration process is expected to occur at depths of ~50–150 km in a cold subduction environment such as that beneath Northeast Japan (Hacker et al., 2003; Iwamori and Zhao, 2000; Kita et al., 2006; Tsuji et al., 2008). Because the presence of water substantially lowers the melting temperature of mantle peridotite, it is generally believed that the liberated water eventually triggers mantle melting, thereby generating island arc volcanism (Tatsumi, 1989). This scheme of dehydration of the subducting slab is petrologically and geodynamically well established (e.g., Kawakatsu and Watada, 2007; Iwamori, 2007); however, it remains unknown as to how and where the oceanic crust becomes hydrated.

In this paper, we document the high-T brittle failure and subsequent hydration-reaction-related sealing of a fault zone within young oceanic crust upon the Atlantis Massif, Mid-Atlantic Ridge (30°10'N; Fig. 1) drilled during Expeditions 304 and 305 of the Integrated Ocean Drilling Program (EXP304/305 IODP; Blackman et al., 2006). The fault zone of interest is located at 746 meters below sea level (mbsf) within massive gabbro suites, and shows no overprinting by exhumation-related structures. A combined study of *in situ* borehole logging data and analyses of drill core recovered from the fault zone enables us to characterize the fault zone. We argue that the documented hydration processes may occur pervasively within oceanic crust along fault zones beneath the mid-oceanic ridge.

2. Geological Setting

The Atlantis Massif, which formed within the past 1.5–2 m.y., bounds the west side of the median valley of the Mid-Atlantic Ridge (Fig. 1). The corrugated,

82 striated central portion of this domal massif displays morphologic and geophysical
83 characteristics inferred to be representative of an oceanic core complex exposed via
84 long-lived detachment faulting (e.g., Cann et al., 1997; Tucholke et al., 1998;
85 Blackman et al., 1998; Collins et al., 2001; Escartin et al., 2003; Blackman et al.,
86 2004). The drill hole analyzed in the present study (EXP304/305 IODP) is located
87 within the footwall of the detachment fault, extending through a succession of
88 gabbroic lithologies down to final depth of 1415 mbsf (Blackman et al., 2006;
89 Ildefonse et al., 2007). The interval between 720 and 780 mbsf, within which the
90 fault zone of the present study occurs, consists of a succession of massive gabbro,
91 olivine gabbro, oxide gabbro, and minor diabase intrusions (Fig. 1). The fault zone
92 consists of three discrete brittle faults, and occurs well below the major detachment
93 fault located at the top of the hole, where brittle and plastic deformation appears to
94 be more intense (Blackman et al., 2006).
95
96 **3. Logging Data**
97
98 *3.1. Methods*
99 Downhole logging data are useful in complementing core data (e.g., visual
100 core descriptions, analysis of thin sections) and determining the orientation of
101 structures identified in the recovered core. The coverage of downhole data attained
102 during EXP 304/305 was almost 100% (Blackman et al., 2006). Standard logs such
103 as density, resistivity, neutron porosity, and natural gamma radiation were collected
104 between depths of 50 and 1415 mbsf at a sampling interval of 0.15 m.
105 Density was measured using the hostile-environment lithodensity tool
106 (HLDT). In this highly resistive environment, a dual laterolog (DLL) was used to
107 measure resistivity, recording both shallow and deep penetrating resistivity. An
108 accelerator porosity sonde (APS) was used to estimate porosity and degree of
109 alteration. In highly altered rocks, neutron porosity shows a marked increase related
110 to the sensitivity of the tool to hydrogen-rich minerals (e.g., clays, chlorite, and
111 serpentinite) that fill veins and occur as replacement minerals. The
112 hostile-environment spectral gamma ray tool (HNGS) and spectral gamma ray tool
113 (NGT) were used to measure natural radioactivity. The HNGS output was generally

114 superior to that of NGT, as it was run first and the rocks were not artificially
115 activated by the neutron porosity tool.
116 Formation microscanner (FMS) electric resistivity images were used to assess
117 variations in structure. The FMS is a four-pad microelectrical resistivity device that
118 enables detailed investigations of vertical and lateral variations in formation
119 resistivity (Serra, 1989) with a shallow depth of investigation (~2 mm). Data quality
120 is highly sensitive to poor pad contact with the borehole wall arising from surface
121 roughness. The obtained resistivity values are relative because the current flow is
122 continuously adjusted during logging to optimize the operating range of the tool
123 under varying bed resistivity. Resistivity measurements are recorded every 2.5 mm,
124 and the vertical resolution of the tool is in the order of 2.5 cm; it is possible to detect
125 beds thinner than 2.5 cm if high resistivity contrast exists between the adjacent beds
126 (Serra, 1989). During data processing, images were dynamically normalized over a 2
127 m moving window.
128
129 *3.2. Logging Results*
130 The quality of the logging data is extremely high for all tools because of the
131 excellent hole conditions encountered during drilling. The density, resistivity, and
132 velocity logs are useful in distinguishing different gabbroic rocks, and are
133 particularly valuable in examining the overall structure, including that in
134 non-recovered sections within the interval around the fault zone. The trends in these
135 datasets are related to alteration and deformation associated with the fault zone (Fig.
136 1).
137 The diameter of the borehole (named as Caliper) varies between 25.46 and
138 31.46 cm (Fig. 1). The maximum diameter occurs in gabbro at 731.8 mbsf, and the
139 minimum in diabase at around 760 mbsf. This interval between 740 and 760 mbsf
140 shows a highly smooth surface, with no apparent breakouts despite the low recovery
141 at certain intervals such as the fault zone.
142 The overall neutron porosity within the borehole is generally around 5%, a
143 typical value for gabbro, although this figure exceeds 10% in places, including the
144 interval containing the fault zone (Fig. 1). The shallow and deep resistivity decrease
145 from 144 ohm.m in regular gabbro to 28 ohm.m within the fault zone (Fig. 1), and

146 density decreases from ~2.9 gr/cm^3 in regular gabbro to ~2.0 gr/cm^3 within the fault
147 zone.
148 Within the fault zone, between 744 and 750 mbsf, the electrical horehole wall
149 images reveal an approximately 1-m interval of east-dipping structures between
150 structures that dip to the north and south (Fig. 1).
151
152 **4. Core Analyses**
153
154 Only 0.8 m of core was recovered from the 4.8 m interval between 746.2 and
155 751.0 mbsf (Fig. 1), with most of the core showing intense brittle deformation
156 indicative of cataclasis and ultracataclasis. This section of core is described in detail
157 below.
158
159 *4.1. Microstructural Analyses*
160 Detailed microstructural observations reveal the occurrence of ultracataclasite
161 within coarse cataclasites (Fig. 2); the ultracataclasite contains local microscopic
162 seams of amphibole (Fig. 2C-F), as described below. The coarse cataclasite contains
163 irregularly shaped clasts of plagioclase and locally amphibole within an altered
164 matrix (Fig. 2B). The coarse plagioclase fragments are fractured and show weak
165 undulose extinction. The amphibole clasts, which are altered clinopyroxene grains,
166 show bending with undulose extinction and microcracks. The altered matrix consists
167 of very fine (<1 mm) amphibole with no apparent shape-preferred orientation. The
168 sizes of plagioclase clasts decrease toward the ultracataclasite zone (Fig. 2B). Within
169 this zone, relic coarse plagioclase clasts show moderate undulose extinction and are
170 intensely fractured, with offset recorded along some of the fractures.
171 Seams of amphibole and minor epidote and plagioclase occur within the
172 ultracataclasite zone. Amphibole (001) cleavages are oriented subparallel to the fault
173 plane. The seams are irregularly distributed, but are most common within the zone
174 with the most fine-grained clasts, which they locally anastomose around or cut across
175 (Fig. 2C–F). These relationships indicate that the seams originated from the
176 syntectonic replacement of clasts during brittle deformation (i.e., development of the
177 fault zone). Furthermore, flow structures around epidote and plagioclase grains (see

178 Fig. 2C–F) indicate that the seams were subsequently plastically deformed, without
179 further brittle deformation.
180
181 *4.2. Mineral Chemistry*
182 *4.2.1. Methods*
183 The chemical compositions of minerals within two polished thin sections (TS
184 #398 and #399) cut from samples from the fault zone were analyzed using a JEOL
185 JXA-733 electron microprobe with three spectrometers housed at Okayama
186 University, Japan. Operating conditions were an accelerating voltage of 15 kV,
187 sample current of 10–20 nA, and a defocused beam of 20 μm diameter. Analyzed
188 standards were natural or synthetic oxides and silicates. The applied matrix
189 correction followed that of Bence and Albee (1968), using the alpha factors of
190 Nakamura and Kushiro (1970).
191 *4.2.2. Results*
192 Representative analyses are listed in Table 1, and the locations of analyzed
193 points are shown in Fig. 3. The fibrous amphibole that forms the thin semas in the
194 ultracataclasite (points A2 and A4 in TS #398; Table 1 and Fig. 3) has the
195 composition of actinolite (Leake, 1978), but is rich in Al and poor in Si (< 7.6 per
196 formula unit) relative to typical greenschist-facies actinolite. Some of the
197 amphibole-like fibrous minerals within the films (points A1, A3, and A5 in TS #398;
198 Table 1 and Fig. 3) have slightly different compositions from the actinolites, being
199 deficient in total oxides (< 93 wt.%); this may reflect a high H_2O content. Under the
200 microscope, these grains have lower relief, lower birefringence, and smaller
201 extinction angles than actinolite. These optical characteristics, in combination with
202 the possible enrichment in H_2O, suggest that the actinolitic seams are partly
203 decomposed to a variety of biopyribole due to low-temperature alteration; however,
204 the invariable nature of the ratio of tetrahedral cations to tetrahedral and octahedral
205 cations, (Si + Al)/(Si + Ti + Al + Fe + Mn + Mg + Ca) (Table 1), suggests that
206 amphibole composition is largely unaffected by alteration (Veblen and Burnham,
207 1978).
208 Fibrous amphibole that coexists with chlorite (point A1 in TS #399; Table 1
209 and Fig. 3) is similar in Si, Al, and alkali contents to the film-forming aluminous

actinolite, whereas amphibole clasts and fringes around chlorite are highly variable in composition (points A2, A3, and A4 in TS #399), suggesting chemical disequilibrium at the thin-section scale and variable physical conditions of amphibole formation. In particular, the high Al and low Si contents of the amphibole clasts suggest that high-temperature metamorphism preceded cataclasis and the formation of ultracataclasite.

Plagioclase grains show a bimodal distribution of compositions related to grain size: anorthite contents [An = 100*Ca/(Ca + Na + K)] are 39–43 and 62–63 in small clasts and large crystals, respectively (Table 1 and Fig. 3). On the basis of textural evidence such as grain size, grain shape, and mode of occurrence, the large plagioclase crystals are considered to be relic crystals that grew at an early stage of igneous crystallization or high-temperature metamorphic crystallization; in contrast, the small clasts formed during brittle deformation associated with chemical adjustment to low-temperature conditions.

Plagioclase clasts embedded in the foliated seams (points P1 and P2 in TS #398) are likely to have formed in equilibrium with the aluminous actinolite, as they are homogeneous in composition and in direct contact with the actinolite (Fig. 3). Using the amphibole–plagioclase thermometer of Holland and Blundy (1994) and assuming a pressure of 200 MPa, we calculated equilibration temperature conditions of about 640 °C for the plagioclase clasts and aluminous actinolite.

5. Permeability Measurements

5.1. Experimental Procedure

Permeability measurements were performed on samples collected across the fault zone (Table 2). For gas permeability measurements, the samples were shaped into cylinders with a diameter of 25 mm and length of ~9 mm (except for one fragile sample which was cut into a rectangular shape of 20 × 20 × 7.1 mm) and then dried at 90 °C in an oven for at least 2 weeks to eliminate pore water. All measurements were conducted using an intra-vessel deformation and fluid-flow apparatus (Hirose and Hayman, 2008). Specimens were jacketed with three layers of polyolefin shrinking tubes to isolate the pores from the confining medium. To evaluate the

evolution of permeability with confining pressure, the pressure was increased in a stepwise manner from 5 MPa up to either 60 or 140 MPa and then decreased back down to 5 MPa (Fig. 4).

In measuring permeability, we used the steady-state flow method with nitrogen gas as a pore-fluid medium. A constant pore-pressure gradient of 0.2–2.4 MPa was applied across the specimen, with the volume of gas flowing through the specimen being monitored by soap-film flowmeters. The permeability value, k, for the nitrogen gas flow is given by the following equation based on Darcy's law:

$$k = \frac{2\eta LQ}{A} \frac{P_{down}}{P_{up}^2 - P_{down}^2},$$

where Q is the flow rate, A is the cross-sectional area perpendicular to the flow direction, L is the specimen length parallel to the flow direction, η is the viscosity of the pore fluid, and P_{up} and P_{down} are the pore pressures in the upper and lower ends of the specimen. The measurable flow rate in the apparatus can be varied from 0.05 to 5000 ml/min, which roughly corresponds to permeabilities ranging from 10^{-21} to 10^{-16} m^2 for specimens of this size.

5.2. Experimental Results

The permeability values obtained for the regular gabbro and fault rocks as a function of confining pressure are shown in Fig. 4A and B, respectively (see also Table 2). The results show the following trends: (1) host rocks are more impermeable than the fault rocks by more than an order of magnitude; (2) permeability decreases with increasing confining pressure, and tends to be lower during the second pressure cycle; (3) for all specimens, the reduced permeability during pressurization did not recover to the initial values during depressurization. For comparison with the borehole data, Fig. 1 shows permeability data at an effective confining pressure of 20 MPa during the downward pressure cycle, which approximately corresponds to the borehole pressure. The downhole permeability plot shows that the fault zone is relatively permeable compared with adjacent rocks, with a permeability of 10^{-18} to 10^{-17} m^2.

6. Interpretation and Discussion

6.1. Logging Data Across the Fault Zone associated with Fault rocks

The 0.8 m of core recovered from the 4.8 m interval between 746.2 and 751.0 mbsf shows intense brittle deformation indicative of cataclasis and ultracataclasis (Fig. 2). Several pieces of ultracataclasite were obtained from sections of gabbro subject to intense brittle deformation within the fault zone (e.g., Fig. 2A). However, it is difficult to determine the scale of the fault zone, since the rate of core recovery was poor across the fault zone (between 744 and 752 mbsf). In contrast, a near-complete set of downhole logging data was obtained (Fig. 1).

The borehole condition was as good quality as the smooth borehole width across the fault zone (Fig. 1), indicating that the fault zone appears to be well lithified in spite of the development of fault rocks. However, the other logging data around the core of the fault rocks are remarkably different from the protolith gabbroic rocks in the interval between 720 and 780 mbsf: i.e., the low deep resistivity, the high gamma ray and the high neutron porosity, suggesting that the fault zone contains conductive phases (Fig. 1). This interpretation is further supported by the density data, which show values of ~2.9 gr/cm^3 in the gabbro suites, decreasing to ~2.0 gr/cm^3 within the fault zone. Although the absolute density is poorly calibrated, this decrease in apparent density might be explained by the relatively high permeability within the fault zone (discussed below) and the presence of hydrous phases such as amphibole. At 745 mbsf, where the borehole width data indicate an absence of breakouts, the density is ~2.0 g/cm^3, suggesting that cracks, if present at all, remain closed.

Moreover, the electrical horehole wall images can be analyzed to obtain information on the geometry of lithological contacts and fractures within the fault zone (Fig. 1). The images reveal a distinct dark region at the top of the east-dipping zone at around 745.5 mbsf, possibly corresponding to the lowest recorded density of 2.0 g/cm^3 and the highest neutron porosity of 26 % (Fig. 1). These structures probably reveal the full extent of the fault zone, which on this basis is more than 5 m wide at around 745 mbsf (Fig. 1).

304 *6.2. Permeability of the fault zone: implication for hyrdration in the oceanic crust*

305 The fault zone consists of cataclasite and ultracataclasite. The ultracataclasite
306 contains seams of amphibole and minor epidote and plagioclase (Fig. 2C–F). Flow
307 structures around epidote and plagioclase grains (Fig. 2C–F) demonstrate that the
308 seams were subsequently plastically deformed, with no apparent brittle deformation.
309 Since these seams appear to have developed at temperatures of around 640 °C (Fig.
310 3), these microstructural development would indicate a high temperature brittle
311 failure and subsequent slow slip in the fault zone in association with hydrothermal
312 alteration.

313 Our laboratory measurements indicate that the permeability of the fault zone
314 is in the order of 10^{-19} to 10^{-17} m^2, more than an order magnitude higher than that of
315 the host gabbroic rocks (Fig. 4). Because our experiments were performed using
316 small cores that did not contain large-scale fractures, much higher permeabilities are
317 likely within the highly fractured parts of the fault zone that were not recovered
318 during drilling. In fact, high permeability, ranging from 10^{-18} to 10^{-13} m^2, has been
319 reported from *in situ* permeability measurements of shallow basaltic oceanic crust
320 within which fractures are favorably developed (see the review by Fisher, 1998).
321 Although large-scale crustal fault zones are likely to be more highly permeable than
322 that indicated by our laboratory results, our relatively low-permeability fault data
323 may represent the permeability structure of minor-scale or locally inactive fault
324 zones such as those likely to be observed within the present cores (Fig. 2). Such a
325 low-permeable fault zone results from progressive sealing via the formation of
326 hydrous minerals at around 640 °C. Given that the amphibole crystals that act as the
327 seal were plastically deformed within the fault zone (Fig. 2), such a low permeability
328 structure within the fault zone, which is as low as that of the lower crust (e.g., Brace,
329 1984), would occur during the later stages or perhaps even the last stage of fault
330 movement (i.e., a post-seismic event).

331 We argue that the low-permeable fault zone observed within gabbro in the
332 present study is one of the best candidate structures for preserving water in the
333 oceanic crust. The water could be input into lower crustal rocks to form hydrous
334 minerals along fault zones that developed near the spreading axis presumably during
335 seismic events (e.g., Wolfe et al., 1995) and might then be preserved because of a

low permeability structure, until dehydration reactions occur with increasing temperature at some tectonic settings such as a subducting slab.

7. Conclusions

IODP EXP304/305 drilled a succession of gabbroic lithologies to a final depth of 1415 meters below the sea floor (mbsf), attaining very high recovery rates of up to 100% (generally ~80%). We identified an intra-crustal fault zone between 720 and 780 mbsf in a section consisting of massive gabbro, olivine gabbro, oxide gabbro, and minor diabase intrusions. Of particular interest is the section between 744 and 750 mbsf, marked by poor core recovery (17%). Electrical borehole-wall images show a 1-m-thick zone of east-dipping fractures within this interval that is otherwise dominated by structures dipping to the N and S. Despite a high fracture density, the section has smooth walls with rare breakouts, suggesting that the poor recovery is due to a change in lithology rather than well conditions. Ultracataclasite formed in the upper amphibolite regime, with infill dominated by amphibole. Logging data suggest that the gabbroic rocks in this interval are rich in hydrous phases, consistent with the increased amounts of amphibole found in the core. Equilibration temperature conditions of about 640 °C (assuming a pressure of 200 MPa) were obtained for plagioclase clasts and aluminous actinolite. Laboratory experiments reveal that the permeability of the fault zone is in the range of 10^{-19} to 10^{-17} m^2. Although the permeability is relatively high within the fault zone, the overall permeability structure is no higher than that in the lower crust; consequently, because brittle failure occurred at high temperatures, the fault zone was subsequently completely sealed with hydrous minerals, thereby preventing further fluid circulation. Such low-permeable fault zone observed within gabbro in the present study is one of the best candidate structures for preserving water in the oceanic crust.

Acknowledgements

This research used samples and data provided by the Integrated Ocean Drilling Program (IODP) and the shipboard parties of Expedition 304/305. We thank C. P. Jaupart and an anonymous reviewer for their valuable comments and A.

368 Stallard for improving the English in the manuscript. We thank the Integrated Ocean
369 Drilling Program for their extraordinary efforts during Exp 304/305. This study was
370 supported by research grants from the Japan Society for the Promotion of Science
371 (JSPS) and the Japan Drilling Earth Science Consortium (J-DESC).
372
373 **References**
374 Barclay, A.H., Toomey, D.R., Solomon, S.C., 2001. Microearthquake characteristics
375 and crustal Vp/Vs structure at the Mid-Atlantic Ridge, 35°N. J. Geophys. Res.
376 106, 2017-2034.
377 Bence, A.E., Albee, A.L., 1968. Empirical correction factors for the electron
378 microanalysis of silicates and oxides. J. Geol. 76, 382-403.
379 Blackman, D.K., Cann, J.R., Janssen, B., and Smith, D.K., 1998. Origin of
380 extensional core complexes: evidence from the MAR at Atlantis Fracture Zone. J.
381 Geophys. Res. 103, 21315-21334.
382 Blackman, D.K., Karson, J.A., Kelley, D.S., Cann, J.R., Früh-Green, G.L., Gee, J.S.,
383 Hurst, S.D., John, B.E., Morgan, J., Nooner, S.L., Ross, D.K., Schroeder, T.J.,
384 Williams, E.A., 2004. Geology of the Atlantis Massif (MAR 30°N): implications
385 for the evolution of an ultramafic oceanic core complex. Mar. Geophys. Res. 23,
386 443–469.
387 Blackman, D.K., Ildefonse, B., John, B.E., Ohara, Y., Miller, D.J., MacLeod, C.J.,
388 and Expedition 304/305 Scientists, 2006, Proceedings of the Integrated Ocean
389 Drilling Program, Volume 304/305: College Station, Texas, Integrated Ocean
390 Drilling Program Management International, Inc.,
391 doi:10.2204/iodp.proc.304305.2006.
392 Brace, W.F., 1984. Permeability of crystalline rocks - new insitu measurements. J.
393 Geophys. Res. 89, 4327-4330.
394 Cann, J.R., Blackman, D.K., Smith, D.K., McAllister, E., Janssen, B., Mello, S.,
395 Avgerinos, E., Pascoe, A.R., Escartin, J., 1997. Corrugated slip surfaces formed
396 at ridge-transform intersections on the Mid-Atlantic Ridge. Nature 385, 329–332.
397 Collins, J.A., Tucholke, B.E., Canales, J.-P., 2001. Structure of Mid-Atlantic Ridge
398 megamullions from seismic refraction experiments and multichannel seismic

399 reflection profiling. Eos, Trans. Am. Geophys. Union 82, F1100.
400 Escartin, J., Mével, C., MacLeod, C.J., McCaig, A.M., 2003. Constrains on
401 deformation conditions and the origin of oceanic detachments: The Mid-Atlantic
402 Ridge core complex at 15°45'N. Geochem. Geophys. Geosyst. 4, 1067,
403 doi:10.1019/2002GC000472, 2003.4
404 Fisher, A.T., 1998. Permeability within basaltic oceanic crust. Rev. Geophys. 36,
405 143-182.
406 Hacker, B.R., Peacock, S.M., Abers, G.A., Holloway, S.D., 2003. Subduction
407 factory: 2. Are intermediate-depth earthquakes in subducting slabs linked to
408 metamorphic dehydration reactions? J. Geophys. Res., 108, 2030,
409 doi:10.1029/2001JB001129.
410 Hirose, T., Hayman, N.W., 2008. Structure, permeability, and strength of a fault zone
411 in the footwall of an oceanic core complex, the Central Dome of the Atlantis
412 Massif, Mid-Atlantic Ridge, 30°N. J. Struct. Geol. 30, 1060-1071.
413 Holland, T., Blundy, J., 1994. Non-ideal interactions in calcic amphiboles and their
414 bearing on amphibole-plagioclase thermometry. Contrib. Miner. Petrol. 116,
415 433-447.
416 Ildefonse, B., Blackman, D.K., John, B.E., Ohara, Y., Miller, D.J., MacLeod, C.J.
417 and Integrated Ocean Drilling Program Expeditions 304/305 Science Party, 2006.
418 Oceanic core complexes and crustal accretion at slow-spreading ridges. Geology,
419 35, 623-626.
420 Iwamori, H., 2007. Transportation of H_2O beneath the Japan arcs and its implications
421 for global water circulation. Chem. Geol. 239, 182-198.
422 Iwamori, H., Zhao, D., 2000. Melting and seismic structure beneath the northeast
423 Japan arc. Geophys. Res. Lett. 27, 425–428.
424 Kawakatsu, H., Watada, S., 2007. Seismic evidence for deep-water transportation in
425 the mantle. Science, 316, 1468, doi: 10.1126/science. 1140855.
426 Kita, S., Okada, T., Nakajima, J., Matsuzawa, T., Hasegawa, A., 2006. Existence of a
427 seismic belt in the upper plane of the double seismic zone extending in the
428 along-arc direction at depths of 70-100 km beneath NE Japan. Geoph. Res. Lett.,
429 33, L24310, doi: 10.1029/2006GL028239.
430 Leake, B.E., 1978. Nomenclature of amphiboles. Mineralogical Magazine, 42,

431 533-563.
432 Nakamura, Y., Kushiro, I., 1970. Compositional relations of coexisting
433 orthopyroxene, pigeonite and augite in a tholeiitic andesite from Hakone volcano.
434 Contrib. Miner. Petrol. 26, 265-275.
435 Peacock, S.M., 1993. Large-scale hydration of the lithosphere above subducting
436 slabs. Chem. Geol., 108, 49–59.
437 Serra, O., 1989. *Formation MicroScanner Image Interpretation:* Houston
438 (Schlumberger Educ. Services), SMP-7028.
439 Tatsumi, Y., 1989. Migration of fluid phases and genesis of basalt magmas in
440 subduction zones. J. Geophys. Res. 94, 4697–4707.
441 Tsuji, Y., Nakajima, J., Hasegawa, A., 2008. Tomographic evidence for hydrated
442 oceanic crust of the Pacific slab beneath northeastern Japan: Implications for
443 water transportation in subduction zones. Geophys. Res. Lett., 35, L15308, doi:
444 10.1029/2008GL034461.
445 Tucholke, B.E., Lin, J., Kleinrock, M.C., 1998. Megamullions and mullion structure
446 defining oceanic metamorphic core complexes on the mid-Atlantic ridge: J.
447 Geophys. Res. 103, 9857–9866, doi:10.1029/98JB00167.
448 Veblen, D.R., Burnham, C.W., 1978. New biopyriboles from Chester, Vermont: I.
449 Descriptive mineralogy. Amer. Mineral., 63, 1000-1009.
450 Wolfe, C.J., Purdy, G.M., Toomey, D.R., Solomon, S.C., 1995. Microearthquake
451 chracteristics and crustal velocity structure at 29 °N on the Mid-Atlantic Ridge:
452 The architecture of a slow spreading segment. J. Geophys. Res. 100,
453 24449-24472.
454

455 Figure captions
456
457 Figure 1.
458 Borehole data for the interval between 720 and 780 mbsf within Hole
459 U1309D drilled by IODP Expeditions 304 and 305. The fault zone occurs in the
460 interval between 746.2 and 751.0 mbsf (colored in yellow), for which permeability
461 measurements were performed. A distinct dark layer occurs at the top of the
462 east-dipping zone at around 745.5 mbsf, from where core was not recovered (colored
463 in pink). See the text for details.
464
465 Figure 2.
466 (A) Ultracataclasite recovered from Core U1309D 152R1 (for sample
467 location within the borehole, see the right-hand side of Fig. 1). An apparent reverse
468 sense of movement (white arrows) is apparent from the geometries of asymmetric
469 fragments. The white rectangle represents the area from which a thin section was
470 made. (B) Microphotograph of the entire thin section cut from the area indicated by
471 the rectangle in A. Width: 3 cm. Cataclasite consists of plagioclase and amphibole
472 fragments in a matrix of amphibole. Black rectangles show the areas enlarged in C
473 and F. (C) Amphibole-dominated films within the ultracataclasite. (D) and (E)
474 Enlargements of the amphibole-dominated films shown in C, showing flow
475 structures around epidote (EP) and plagioclase grains. (F) Enlargement of the
476 amphibole-dominated films shown in B. Very fine-grained fragments were replaced
477 by the amphibole films.
478
479 Figure 3.
480 Points selected for EPMA analysis shown on a BEI image of the amphibole
481 films shown in Fig. 2C. A: amphibole, Pl: plagioclase, E: epidote. Representative
482 results of the analyses are listed in Table. 1.
483
484 Figure 4.
485 Gas permeability data as a function of effective pressure for host rocks (A)

and fault rocks (B) (see Table 2 for summary). Data are the average values of four measurements. Error bars are smaller than the data symbols.

Figure

Click here to download Figure: Figures.doc

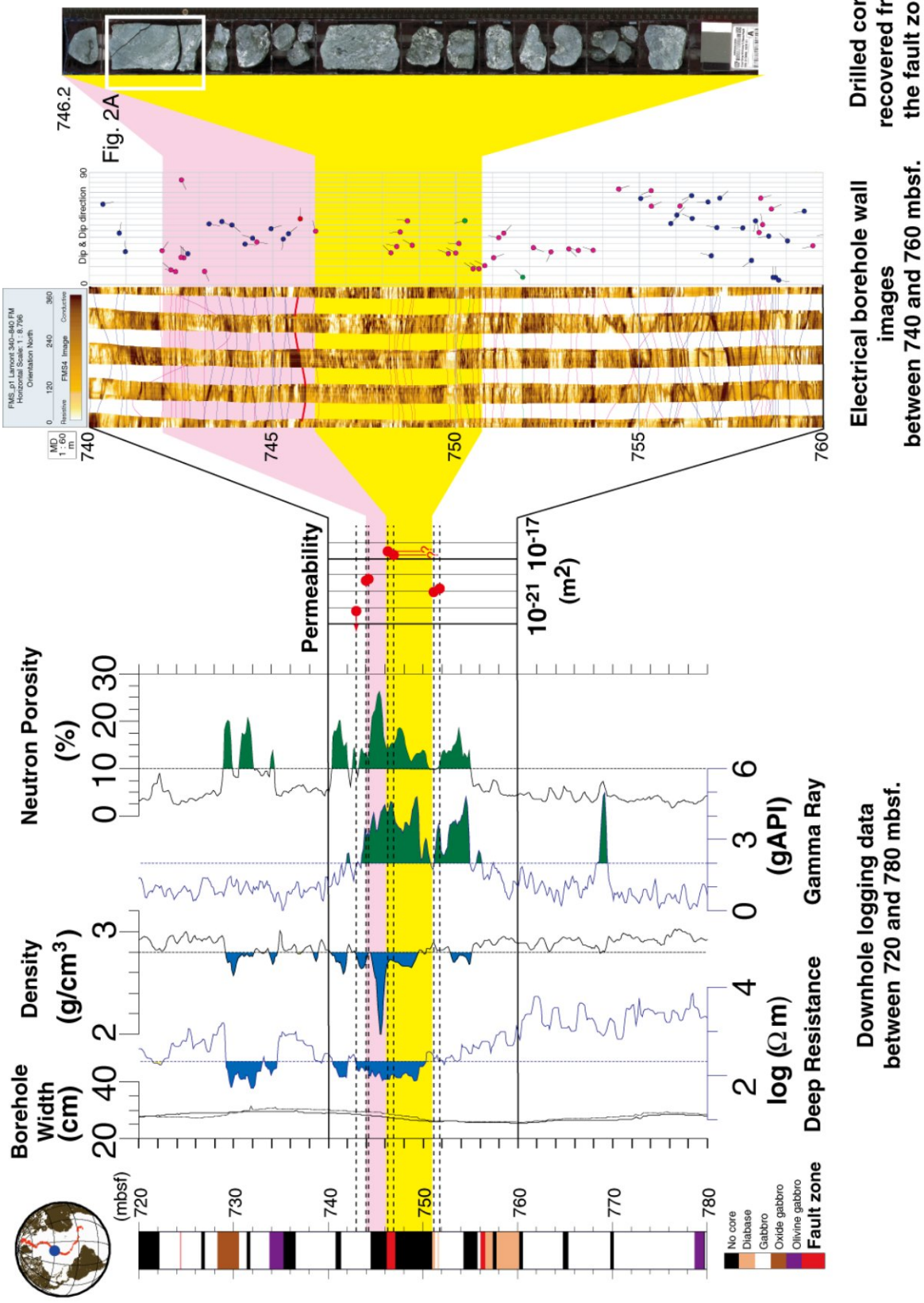

Figure 1: Michibayashi et al.

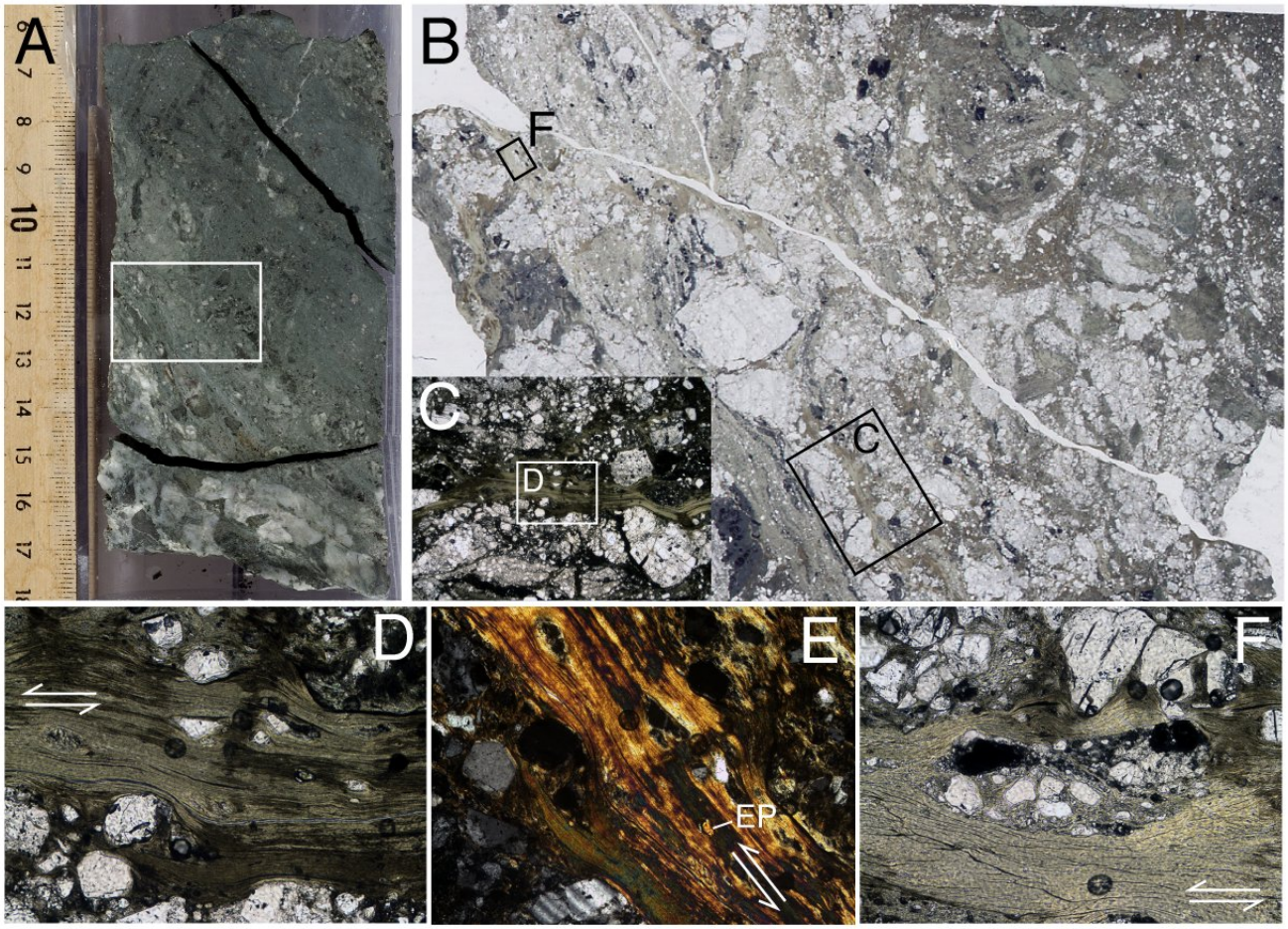

Figure 2. (A) Ultracataclasite recovered from Core U1309D 152R1 (for sample location within the borehole, see the right-hand side of Fig. 1). An apparent reverse sense of movement (white arrows) is apparent from the geometries of asymmetric fragments. The white rectangle represents the area from which a thin section was made. (B) Microphotograph of the entire thin section cut from the area indicated by the rectangle in A. Width: 3 cm. Cataclasite consists of plagioclase and amphibole fragments in a matrix of amphibole. Black rectangles show the areas enlarged in C and F. (C) Amphibole-dominated films within the ultracataclasite. (D) and (E) Enlargements of the amphibole-dominated films shown in C, showing flow structures around epidote (EP) and plagioclase grains. (F) Enlargement of the amphibole-dominated films shown in B. Very fine-grained fragments were replaced by the amphibole films.

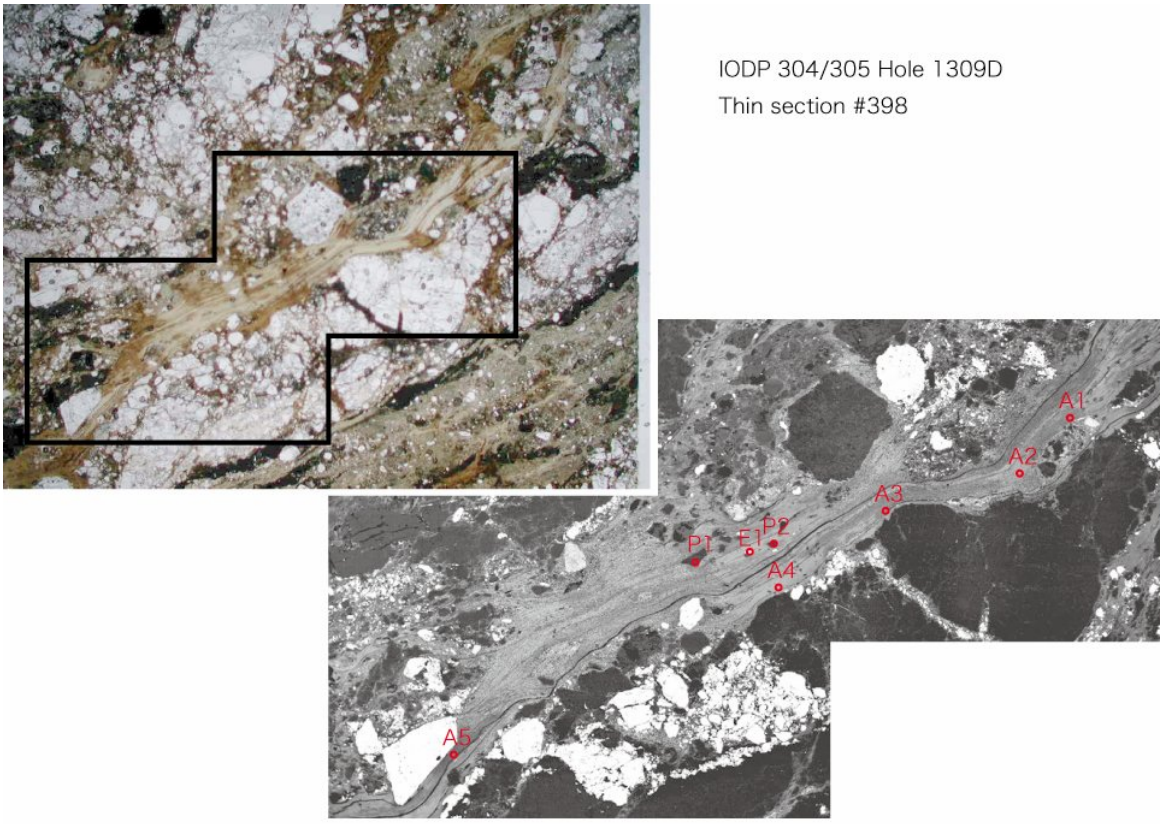

Figure 3. Points selected for EPMA analysis shown on a BEI image of the amphibole films shown in Fig. 2C. A: amphibole, Pl: plagioclase, E: epidote. Representative results of the analyses are listed in Table. 1.

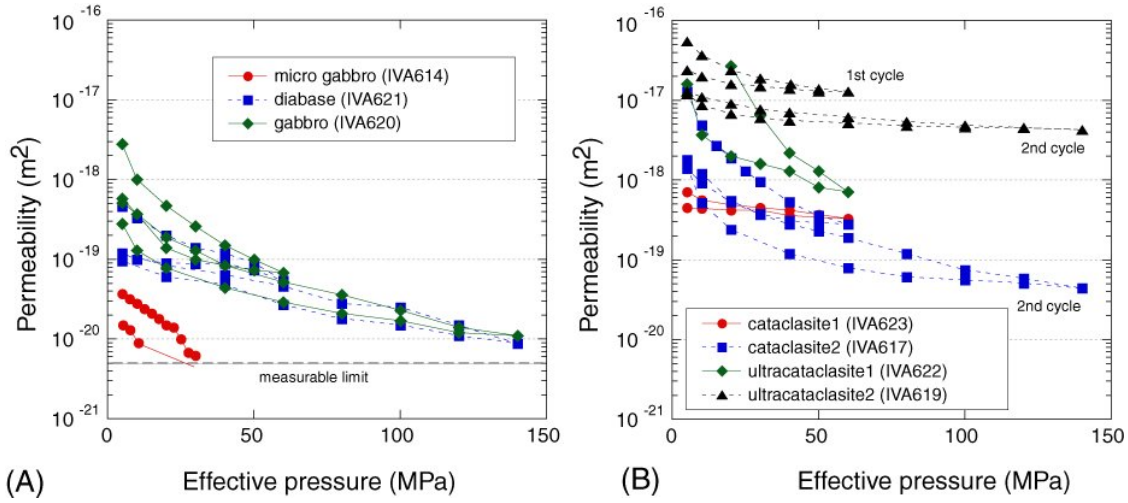

Figure 4. Gas permeability data as a function of effective pressure for host rocks (A) and fault rocks (B) (see Table 2 for summary). Data are the average values of four measurements. Error bars are smaller than the data symbols.

Table

Click here to download Table: Tables.doc

Table 1. Chemical compositions of minerals.

Thin Section No.	398	398	398	398	398	398	398	398	399	399	399	399	399	399	399	399	399	399
Sample No.	A1	A2	A3	A4	A5	E1	Pl1	Pl2	Chl1	Chl2	Am1	Am2	Am3	Am4	Pl1	Pl2	Pl3	Pl4
SiO2	49.76	52.06	49.77	51.66	47.94	35.55	57.77	58.17	26.00	26.12	51.18	49.89	46.97	51.84	52.14	51.76	57.48	57.65
TiO2	0.17	0.17	0.16	0.17	0.11	0.07	nd	nd	0.06	0.07	0.34	0.31	0.82	0.09	nd	nd	nd	nd
Al2O3	3.39	3.69	3.47	3.99	3.83	22.11	27.26	27.05	19.60	19.36	2.76	5.36	5.92	1.38	28.81	28.57	25.10	25.25
FeO*	12.17	12.93	12.80	13.51	13.85		nd	nd	23.19	23.03	19.55	17.16	24.81	21.46	nd	nd	nd	nd
Fe2O3**						13.36												
MnO	0.15	0.21	0.22	0.29	0.23	0.16	nd	nd	0.21	0.22	0.39	0.14	0.79	0.58	nd	nd	nd	nd
MgO	15.15	15.87	14.62	15.59	13.99	0.11	nd	nd	17.80	18.24	11.66	12.46	8.83	11.53	nd	nd	nd	nd
CaO	11.22	11.69	11.06	10.89	10.02	19.63	8.56	8.57	0.08	0.12	11.91	12.26	9.48	11.41	12.99	13.13	8.66	8.84
Na2O	0.32	0.40	0.36	0.48	0.61	0.00	6.64	7.47	0.00	0.01	0.30	0.65	1.03	0.21	4.26	4.22	6.60	6.55
K2O	0.04	0.04	0.03	0.07	0.06	0.04	0.08	0.07	0.01	0.02	0.05	0.04	0.12	0.06	0.06	0.04	0.10	0.08
total	92.37	97.06	92.49	96.65	90.64	91.03	100.31	101.33	86.95	87.19	98.14	98.27	98.77	98.56	98.26	97.72	97.94	98.37
Cations/O=	23	23	23	23	23	12.5	8	8	7	7	23	23	23	23	8	8	8	8
Si	7.578	7.555	7.591	7.539	7.510	3.029	2.576	2.576	1.369	1.371	7.600	7.329	7.133	7.725	2.407	2.404	2.627	2.624
Ti	0.020	0.018	0.018	0.018	0.014	0.004	nd	nd	0.002	0.003	0.038	0.034	0.094	0.010	nd	nd	nd	nd
Al	0.609	0.631	0.623	0.687	0.706	2.220	1.433	1.412	1.216	1.198	0.484	0.928	1.060	0.243	1.567	1.564	1.352	1.354
Fe	1.550	1.570	1.633	1.649	1.815	0.856	nd	nd	1.021	1.011	2.428	2.108	3.150	2.674	nd	nd	nd	nd
Mn	0.019	0.026	0.029	0.036	0.030	0.012	nd	nd	0.010	0.010	0.049	0.017	0.102	0.074	nd	nd	nd	nd
Mg	3.440	3.434	3.325	3.392	3.268	0.014	nd	nd	1.397	1.427	2.581	2.729	1.998	2.561	nd	nd	nd	nd
Ca	1.830	1.818	1.806	1.703	1.681	1.810	0.409	0.407	0.004	0.007	1.894	1.929	1.543	1.822	0.642	0.654	0.424	0.431
Na	0.094	0.112	0.106	0.136	0.186	0.000	0.574	0.641	0.000	0.001	0.086	0.186	0.303	0.060	0.381	0.380	0.584	0.578
K	0.008	0.007	0.005	0.013	0.011	0.004	0.004	0.004	0.001	0.002	0.009	0.008	0.023	0.011	0.004	0.002	0.006	0.005
Total	15.148	15.171	15.136	15.173	15.221	7.950	4.996	5.040	5.020	5.030	15.169	15.268	15.406	15.180	5.001	5.004	4.993	4.992
Mg#	68.9	68.6	67.1	67.3	64.3				57.8	58.5	51.5	56.4	38.8	48.9				
An							41.4	38.7							62.5	63.1	41.8	42.5
SA/STAFMMC	0.54	0.54	0.55	0.55	0.55						0.54	0.55	0.54	0.53				

Pl = plagioclase, Chl = chlorite, Am = amphibole, A = amphibole or amphibole-like phase, E = epidote or epidote-like phase

* total iron as FeO

** total iron as Fe2O3

nd = not determined

Mg# = 100*Mg/(Mg+Fe)

An = 100*Ca/(Ca+Na+K)

SA/STAFMMC = (Si+Al)/(Si+Ti+Al+Fe+Mn+Mg+Ca)

Table 2. Summary of laboratory-derived permeability data reported in this study.

core	section	interval		mbsf	lithology	run no.	confining pressure (Pc) path MPa	pore pressure (Pp) MPa	Permeability at Pc of 20 MPa * m2	remarks
151	2	36	39	743	micro gabbro	IVA614	5-60-5	2.4	6.0E-21	lower than measurable limit
	2	101	103	744	cataclasite1	IVA623	5-60-5	2.4	4.2E-19	
	3	1	3	744.3	cataclasite2	IVA617	5-60-5-140-5	0.2-2.4	2.4E-19	2 Pc cycles, test with different Pp
152	1	7	11	746.3	ultracataclasite1	IVA622	5-60-5	2.4	2.7E-17	rectangular shape sample
	1	75	77	745	ultracataclasite2	IVA619	5-60-5-140-5	0.3-2.4	6.8E-18	2 Pc cycles, test with different Pp
153	1	20	23	751.2	diabase	IVA621	5-60-5-140-5	2.4	6.1E-20	2 Pc cycles
	1	75	77	751.8	gabbro	IVA620	5-60-5-140-5	2.4	7.8E-20	2 Pc cycles

* Permeability data at second depressurization path with pore pressure of 2.4 MPa